

Optoelectronic Properties and Defect Physics of Lead-Free Photovoltaic Absorbers $\text{Cs}_2\text{Au}^{\text{I}}\text{Au}^{\text{III}}X_6$ ($X = \text{I}, \text{Br}$)

Jiban Kangsabanik, Supriti Ghorui, M. Aslam, and Aftab Alam[✉]*

Department of Physics, Indian Institute of Technology Bombay, Powai, Mumbai 400076, India



(Received 26 March 2019; revised manuscript received 25 October 2019; published 6 January 2020)

Stability and toxicity issues with the hybrid lead iodide perovskite MAPbI_3 necessitate a hunt for potential alternatives. Here, we shed light on promising photovoltaic properties of gold mixed-valence halide perovskites $\text{Cs}_2\text{Au}_2X_6$ ($X = \text{I}, \text{Br}, \text{Cl}$). They satisfy fundamental requirements such as nontoxicity, better stability, a band gap in the visible range, and a low excitonic binding energy. Our study shows a favorable electronic structure, resulting in a high optical-transition strength, and thus a sharp rise in the absorption spectrum near the band gap. This, in turn, yields a very high short-circuit current density and hence higher simulated efficiency compared with MAPbI_3 . However, careful investigation of defect physics reveals the possibility of deep-level defects (such as V_X , V_{Cs} , X_{Au} , X_{Cs} , Au_i , and Au_X , $X = \text{I}, \text{Br}$), depending on the growth conditions. These can act as carrier traps and become detrimental to photovoltaic performance. The present study should help in taking necessary precautions in synthesizing these compounds in a controlled chemical environment, which should minimize performance-limiting defects and pave the way for future studies on this class of materials.

DOI: 10.1103/PhysRevApplied.13.014005

I. INTRODUCTION

Since its inception in 2009, hybrid lead halide perovskite has become the center of attention in the photovoltaic community. High optical absorption and defect tolerance made its efficiency as high as 22.1%, almost comparable to that of commercial silicon solar cells [1–3]. Despite being highly efficient, it still has not been commercialized to date, mainly due to two reasons, (i) poor stability in the ambient environment and (ii) toxicity due to Pb. Replacing the organic cation with inorganic Cs has helped with stability, but the presence of Pb has seemed unavoidable until now. Many materials have been proposed as alternatives, but either they were even more unstable or the efficiency was low [4–7]. One of the key alternatives which emerged recently is double perovskite halides, $A_2BB'X_6$ [8], where A is Cs, X is one of the halogens, and B, B' are +1, +3 elements. There exist various theoretical and experimental studies exploring different B, B' combinations, but most of these compounds either have an indirect band gap (leading to higher recombination loss) or have a gap in the high violet region due to an optically forbidden transition (leading to poor absorption) [9–11]. A solution has been reported showing an indirect-to-direct transition, but toxicity was still a concern [12–14].

$\text{Cs}_2\text{Au}_2X_6$ ($X = \text{I}, \text{Br}, \text{Cl}$) is a class of compounds which show semiconducting behavior under ambient

conditions [15,16]. Although the predicted band gaps for these materials are quite favorable for solar absorption, they have never been investigated from the photovoltaic perspective. Very recently, Debbichi *et al.* [17] reported a theoretical study of $\text{Cs}_2\text{Au}_2\text{I}_6$ and proposed it as a promising photovoltaic absorber. This was further confirmed by Giorgi *et al.* [18], who showed the presence of weakly bound excitons in this compound (similarly to MAPbI_3), hinting at good photovoltaic performance. However, a few key points were not properly addressed in these studies, e.g., (i) the nature of the band gap and (ii) estimation of the solar efficiency. In addition, these studies focused only on the compound $\text{Cs}_2\text{Au}_2\text{I}_6$, although the other halide compounds also have a band gap in the visible range. Apart from these, the defect physics of these compounds has never been studied. This is extremely important because defects in photovoltaic materials play a crucial role in dictating the device efficiency. For example, the presence of a deep-level defect, which can act as an electron-hole recombination center, limits carrier diffusion to a great extent [19]. While synthesizing a compound, it is therefore very important to create a chemical environment which minimizes the defect concentration in the compound.

In this paper, we perform a detailed first-principles calculation to study the electronic, structural, and optical properties of the full series $\text{Cs}_2\text{Au}_2X_6$ ($X = \text{I}, \text{Br}, \text{Cl}$) from the perspective of photovoltaic applications. Careful analysis of the band structure reveals a slightly indirect nature

*aftab@iitb.ac.in

of the band gap, in contrast to earlier reports [17,18]. However, the optically allowed direct band gap remains within a few meV of the electronic gap, resulting in exciting optoelectronic behavior. The chemical, mechanical, and dynamical stability of all the compounds is also studied. In addition, we investigate the possibility of point-defect formation in various growth environments and find that even under anion-rich conditions, there is the possibility of the formation of deep-level halide vacancies in $\text{Cs}_2\text{Au}_2\text{X}_6$. In addition, a few other deep-level defects are likely to form, depending on the material and chemical environment, which may hinder the performance of the material as a photovoltaic absorber. Additionally, we also simulate a series of compounds with organic cations in place of Cs, i.e., MA ($(\text{CH}_3\text{NH}_3^+)$) and FA ($(\text{CH}(\text{NH}_2)_2^+)$), and investigate the possibility of their formation and their potential as photovoltaic absorbers. All the calculations are done by employing first-principles density-functional theory (DFT) [20] as implemented in the Vienna Ab-initio Simulation Package (VASP) [21,22]. Other details of the calculations are given in Appendix A.

II. STRUCTURAL DETAILS AND STABILITY

Under ambient conditions, $\text{Cs}_2\text{Au}_2\text{X}_6$ ($X = \text{I}, \text{Br}, \text{Cl}$) crystallizes in a double perovskite structure with space group $I4/mmm$ (No. 139). In this structure, the Cs atoms sit at the $4d$ Wyckoff site, the Au(1) and Au(2) atoms sit at sites $2b$ and $2a$, respectively, and the anions sit at two inequivalent sites, $4e$ [$\text{X}(1)$] and $8h$ [$\text{X}(2)$]. Here Au(1) and Au(2) possess oxidation states +1 and +3, respectively, making it possible to have all the features of a double perovskite. The halogens form alternate linear $[\text{Au}(1)\text{X}_2]^-$ and square-planar $[\text{Au}(2)\text{X}_4]^-$ complexes [15,16]. The presence of alternately arranged elongated and compressed AuI_6 octahedra can be seen in Fig. 1(a), and can be confirmed from the respective Au—X bond lengths (see the Supplemental Material [23]), which match well with previous experimentally reported data [24].

First, we check the chemical, mechanical, and dynamical stability of these compounds. For the chemical stability, we calculate the formation enthalpy (ΔH_f) against the binary halides with the following pathway: $M_2\text{Au}_2\text{X}_6 \rightarrow 2MX + \text{AuX} + \text{AuX}_3$ ($M = \text{Cs, MA, FA, } X = \text{I, Br, Cl}$). The results are presented in Table I (for inorganic compounds). Going in the direction $\text{I} \rightarrow \text{Br} \rightarrow \text{Cl}$, the chemical stability increases. For the mechanical stability, we calculate the elastic constants (tabulated in the Supplemental Material [23]), which satisfy the Born-Huang mechanical-stability criteria for all three halides [26]. The calculated phonon dispersions (shown in the Supplemental Material [23]) show no imaginary frequencies, and hence confirm the dynamical stability.

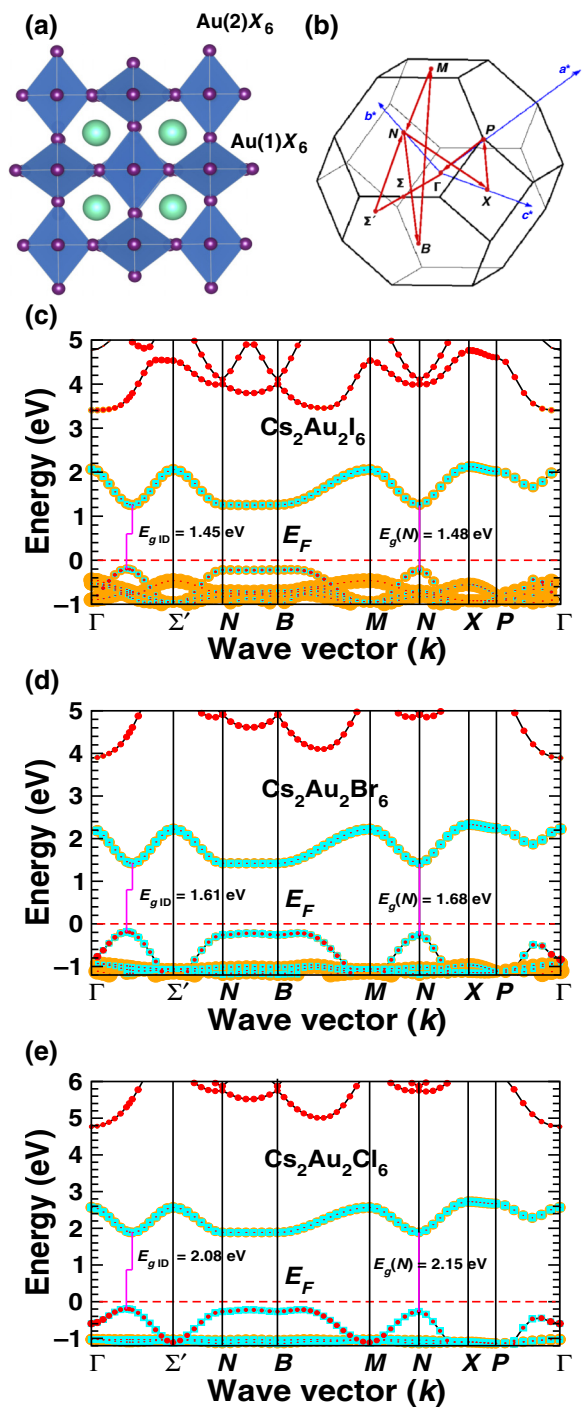


FIG. 1. (a) Crystal structure and (b) 3D Brillouin zone of $\text{Cs}_2\text{Au}_2\text{X}_6$, $X = \text{I, Br, Cl}$. (c)–(e) show the Heyd-Scuseria-Ernzerhof (HSE06) electronic band structures of $\text{Cs}_2\text{Au}_2\text{X}_6$, $X = \text{I, Br, Cl}$, respectively, with the band gap shifted to the HSE06- G_0W_0 calculated value. Orange, turquoise, and red symbols indicate $\text{I} p$, $\text{Au} d$, and $\text{Au} s$ orbital character, respectively.

III. ELECTRONIC STRUCTURE

Figures 1(c)–1(e) show the electronic band structure calculated using a hybrid (HSE06) functional [27] for the

TABLE I. Formation enthalpy (ΔH_f), simulated and experimental band gap (E_g), difference between electronic and optically allowed direct gap (ΔE_g^{da}), short-circuit current density (J_{SC}), open-circuit voltage (V_{OC}), current density (J_{max}) and voltage (V_{max}) at maximum power, spectroscopic limited maximum efficiency (SLME), and fill factor (FF) at 298 K for the three compounds. Various device-related parameters are calculated for a film thickness of 500 nm. For comparison, relevant data for MAPbI_3 are also tabulated.

Compound	ΔH_f (meV/atom)	E_g (eV) HSE06+GW	E_g (eV) (Expt.) ^a	ΔE_g^{da} (meV)	J_{SC} (mA/cm ²)	J_{max} (mA/cm ²)	V_{OC} (V)	V_{max} (V)	SLME (η%)	FF
$\text{Cs}_2\text{Au}_2\text{I}_6$	-66.75	1.45	1.31	13.3	33.02	32.15	1.04	0.95	30.41	0.89
$\text{Cs}_2\text{Au}_2\text{Br}_6$	-109.97	1.61	1.60	17.1	22.90	22.43	1.31	1.21	27.19	0.91
$\text{Cs}_2\text{Au}_2\text{Cl}_6$	-138.14	2.08	2.04	16.2	12.20	12.01	1.72	1.62	19.40	0.92
MAPbI_3	-71.65	1.72 (SS- G_0W_0) ^b	1.50 ^c	0	16.76	16.40	1.27	1.17	19.21	0.90

^a[15].

^b[25].

^c[3].

three compounds. $\text{Cs}_2\text{Au}_2\text{I}_6$ forms an intermediate band composed mainly of the Au(2) $5d_{x^2-y^2}$ and I p orbitals, which is responsible for its band gap (1.31 eV) in the visible range [18,28]. The valence-band maximum (VBM) consists mainly of the Au(1) $5d_{z^2}$ and I p orbitals. In the case of Br and Cl, the orbital contributions seem to be similar, but the band gap increases due to an increase in the nearest-neighbor Coulomb interaction and Jahn-Teller distortion [15]. For better accuracy, we use the HSE06 functional to simulate the band-edge information, whereas the band-gap values are calculated using quasiparticle G_0W_0 calculations starting from wave functions obtained using the HSE06 functional. Our calculation reveals that all these materials have a slightly indirect band gap, having the VBM and conduction-band minimum (CBM) at different points along the Γ -to- Σ' direction, in contrast to previous reports [17,18], where a direct band gap is predicted at the high-symmetry N point. This might be due to the fact that a more detailed Brillouin-zone sampling (i.e., considering an important Γ - Σ' direction in the band structure, where the actual VBM and CBM lie) is done in our study. We also calculate the dipole transition matrix elements (a.k.a. transition probabilities), showing an allowed optical transition at the direct band gap (see Fig. S3 in the Supplemental Material [23]). The high transition strength, indicating the possibility of high absorption, can be attributed to the mixing of halogen p and Au d orbitals [29]. Table I shows our simulated band gap along with the difference between the indirect and the optically allowed direct gap (ΔE_g^{da}). Incorporation of spin-orbit coupling does not have any significant effect on the optoelectronic properties of $\text{Cs}_2\text{Au}_2\text{I}_6$ [the band gap (E_g) changes by 0.07 eV and ΔE_g^{da} remains the same]. This, in turn, implies a negligible change in simulated efficiency. That is why we do not use spin-orbit coupling in our calculation for the other compounds, for which the effects are expected to be even less. Our simulated band gaps match fairly well with previously reported experimental values [15]. We also check the properties of organic cations, namely the MA and FA counterparts

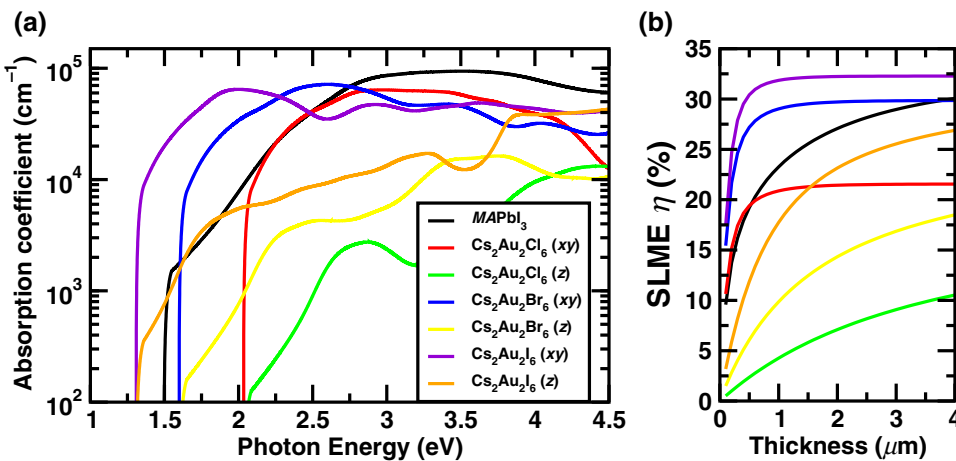
of these compounds. Our calculated lattice parameters for $\text{MA}_2\text{Au}_2\text{I}_6$ agree well with previous experimental data [30]. All the other electronic-structure data, along with the band structure and transition probabilities, are shown in the Supplemental Material [23]. All the organic mixed-valence gold perovskite compounds show a fairly large band gap, restricting their application as photovoltaic absorbers.

IV. ABSORPTION COEFFICIENT AND SPECTROSCOPIC LIMITED MAXIMUM EFFICIENCY

The finite values of the calculated transition probability encourage us to simulate the next relevant parameters for photovoltaic applications, i.e., the absorption coefficients and the SLME. Details of the formulation of the SLME are given in the Supplemental Material [23]; this is a better indicator of photovoltaic efficiency than the bare Shockley-Queisser limit.

Figures 2(a) and 2(b) show the absorption coefficients (α) and the SLME for the three systems. For comparison, corresponding simulated data for MAPbI_3 are also shown. From Fig. 2(a), one can see that the absorption coefficients in the xy plane are an order of magnitude higher than those in the z direction, confirming the strong optical anisotropy of the materials [17,18]. This gives us an idea about the appropriate alignment of the crystal axes so as to maximize the photoabsorption. Careful analysis reveals that the first optical peak in the xy direction can be attributed to a vertical transition between the two highest valence states [comprising mainly Au(1) $5d_{z^2}$ orbitals] and the two lowest conduction states [Au(2) $5d_{x^2-y^2}$ and I p_z orbitals], whereas along the z direction it is due to a transition from the lower part of the valence band [Au(1) $5d_{xz,yz}$] to the intermediate band, explaining the significantly higher optical absorption in the xy plane [18].

Looking at the absorption spectra, one can see a sharp rise in the absorption coefficient (α) near the band gap for all three halides. Although in the lower-wavelength region



the absorption coefficient is higher for MAPbI₃, a lower band gap (for Cs₂Au₂I₆) and a sharper rise in the absorption spectrum near the band edge for both the iodide and the bromide compounds indicate better utilization of the solar spectrum. This is further confirmed by our simulated short-circuit current density (J_{SC}). For completeness, we tabulate the room-temperature (298 K) simulated values of a few important device parameters, such as J_{SC} , the open-circuit voltage (V_{OC}), the current density (J_{max}) and voltage (V_{max}) at maximum power output, the SLME, and the fill factor for a film thickness of 500 nm for all three halides in Table I, and compare these with the values for MAPbI₃. Notice that J_{SC} and J_{max} are almost twice as much for Cs₂Au₂I₆ as for MAPbI₃, and this factor becomes almost 1.5 times at the saturation thickness. The slightly lower attainable voltage makes the efficiency 1.5 times higher at lower film thicknesses, and at least 3% higher at the saturation thickness. A slightly higher band gap causes Cs₂Au₂Br₆ to have a higher attainable voltage, making the SLME much higher than for MAPbI₃ at lower film thicknesses, while the attainable voltage becomes comparable when the thickness is near saturation (see Fig. 2). For Cl, the efficiency remains much lower than for the other two halides, mainly due to the higher band gap, resulting in a much lower attainable current.

V. DEFECT PHYSICS

Defects play a major role in dictating the carrier mobility, lifetime, and recombination rate for a given semiconductor. Unlike extended defects (e.g., grain boundaries and surface passivation), intrinsic point defects (vacancies, interstitials, antisites, etc.) are very difficult to control [19,31,32]. For example, in the case of MAPbI₃, shallow dominant point defects [33] result in a high carrier diffusion length, aiding its high efficiency, whereas the presence of deep-level defects, acting as Shockley-Read-Hall (SRH) recombination centers, is known to be one of the main reasons behind the significantly lower efficiency in the case

FIG. 2. (a) Absorption coefficient vs incident photon energy and (b) SLME vs film thickness at 298 K for Cs₂Au₂X₆, $X = I, Br, Cl$, in the xy plane and z direction. For comparison, simulated results for state-of-the-art MAPbI₃ are also plotted.

of kesterite (CZTS) solar cells [31]. In order to gain better insight, we perform a detailed *ab initio* study of all the possible point defects in Cs₂Au₂I₆ and Cs₂Au₂Br₆, which are predicted to have a theoretical efficiency comparable to or higher than that of MAPbI₃.

The formation energy for a defect D in a charge state q is defined as

$$E^{\text{form}}[D^q] = E^{\text{tot}}[D^q] - E^{\text{tot}}[\text{bulk}] - \sum_i n_i \mu_i + q(E_{\text{VBM}} + \Delta E_F) + E_c, \quad (1)$$

where $E^{\text{tot}}[D^q]$ is the total energy for a supercell with the associated defect D in the charge state q . $E^{\text{tot}}[\text{bulk}]$ is the total energy for a pure bulk supercell of equivalent size. μ_i is the chemical potential of the associated defect, with n_i being the number of defects added ($n_i > 0$) or removed ($n_i < 0$). The next term accounts for the chemical potential of electrons added ($q < 0$) or removed ($q > 0$) to create various charged defect states. E_{VBM} is the energy at the valence-band maximum, and ΔE_F can be varied from 0 (at the VBM) to the band gap E_g (at the CBM). E_c is a correction term, which includes electrostatic and potential-alignment corrections for charged defects [34]. We also include a correction for band-gap underestimation by the Perdew-Burke-Ernzerhof (PBE) exchange-correlation functional [35], via incorporating the band-edge (both VBM and CBM) shifts obtained by more accurate quasiparticle G_0W_0 calculations [36]. More details of the band-gap corrections are provided in Appendix B.

Three types of defects are considered, vacancies ($V_{\text{Cs}}, V_{\text{Au}}, V_X$), interstitials ($\text{Cs}_i, \text{Au}_i, X_i$), and antisites ($\text{Cs}_{\text{Au}}, \text{Cs}_X, \text{Au}_{\text{Cs}}, \text{Au}_X, X_{\text{Cs}}, X_{\text{Au}}$) ($X = I, Br$). Two inequivalent Wyckoff positions are considered for both X and Au. To accurately calculate the various defect charge-state energies, a 160-atom supercell is used. Further discussions of the choice of defects are presented in Appendix C.

It is extremely important to notice that $E^{\text{form}}(D^q)$ can vary depending on the particular choice of μ . Experimentally, this chemical potential can vary depending on the growth environment. The choice of μ generally depends on the stability of the compound against possible elemental and/or competing secondary phases. As secondary phases, we consider the most stable binary halides and other superordered structures of the cations.

First, for the compound to be stable, the thermodynamic equilibrium below must be reached:

$$2 \Delta\mu_{\text{Cs}} + 2 \Delta\mu_{\text{Au}} + 6 \Delta\mu_X = \Delta H_f \quad (X = \text{Br}, \text{I}). \quad (2)$$

Here, ΔH_f is the formation enthalpy of the compound against its elemental constituents. $\Delta\mu_i = \mu_i - \mu_i^0$, where μ_i^0 is the total energy of constituent i in its elemental phase. The following are a set of equations which must be satisfied to avoid coexistence of elemental and secondary phases:

$$\Delta\mu_i < 0, \quad i = \text{Cs, Au, } X, \quad (3)$$

$$a \Delta\mu_{\text{Cs}} + b \Delta\mu_{\text{Au}} + c \Delta\mu_X < \Delta H_f (\text{Cs}_a \text{Au}_b X_c), \quad (4)$$

where $a, b, c = 0, 1, 2, \dots, Z$.

Figures 3(a) and 3(b) shows the phase diagrams for $\text{Cs}_2\text{Au}_2\text{I}_6$ and $\text{Cs}_2\text{Au}_2\text{Br}_6$ against their possible competing elemental and secondary compound phases (taken from the Materials Project database [37]). The brown-shaded areas in both figures show the allowed chemical-potential regions for the constituents, where the intended material is stable. We take seven different sets of allowed chemical potentials for each halogen (shown as points A, B, C, D, E, F, G in the respective diagrams), which represent various chemical environments, from cation-poor and anion-rich to cation-rich and anion-poor conditions. We draw the respective defect-formation-energy diagram for each of them. The related $\Delta\mu_i$ values and

corresponding defect-formation-energy plots can be found in the Supplemental Material [23].

Figures 4 and 5 show the defect formation energies for various intrinsic defects as a function of the Fermi level for three different chemical growth conditions, (a) cation poor and anion rich, (b) cation rich and anion poor, and (c) moderate cations and anions, for $\text{Cs}_2\text{Au}_2\text{I}_6$ and $\text{Cs}_2\text{Au}_2\text{Br}_6$, respectively. The three phases are marked as points A, E (D for $X = \text{Br}$), and G in the respective phase diagrams in Fig. 3, and corresponding $\Delta\mu$ values can be found in the Supplemental Material [23]. The most probable defects (setting a cutoff of $E^{\text{form}}[D^q] \sim 0.75$ eV) are highlighted with respect to the Fermi-level pinning in these figures. We also consider a few other possible growth environments (points $A-G$ in Fig. 3), whose defect formation energies are shown in the Supplemental Material [23]. The line styles (and symbols) for various defects, in all three growth environments, are shown in the right-hand panels of Figs. 4(c) and 5(c). For $\text{Cs}_2\text{Au}_2\text{I}_6$, in a cation-poor and anion-rich environment [Fig. 4(a)], the dominant acceptor-type defects are V_{Cs} and $V_{\text{Au}(1)}$ ($I_{\text{Au}(1)}$ will act as a neutral defect at this Fermi-level pinning), whereas V_{I} and $\text{Au}(1)_i$ are the dominant donors. There is another neutral defect, $\text{Au}(1)_{\text{Cs}}$, which can form at a high concentration, but because it does not show any charge-state transition in the band gap, the Fermi level will be pinned at almost the middle of the gap, where V_{Cs} and $V_{\text{I}(1)}$ intersect. In a cation-rich and anion-poor environment [Fig. 4(b)], donor defects (mostly iodine vacancies) are likely to drag the Fermi level closer to the CBM, where the main acceptor defects will be cation [$\text{Cs, Au}(1)$] vacancies and $I_{\text{Au}(1)}$. Under these growth conditions, the material will show a low n -type carrier concentration. Under moderate cation and anion conditions [Fig. 4(c)], the Fermi-level pinning will be at a position near the midgap region, indicating a very low intrinsic carrier concentration. Overall, one can see that iodine vacancies (along with V_{Cs}) are the most dominant defects under all growth conditions,

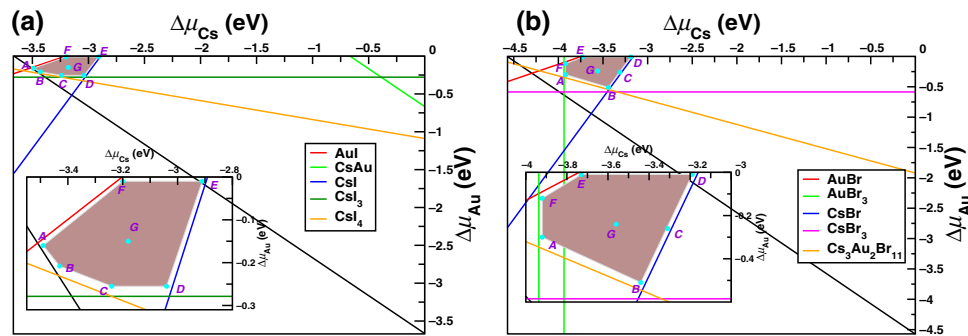
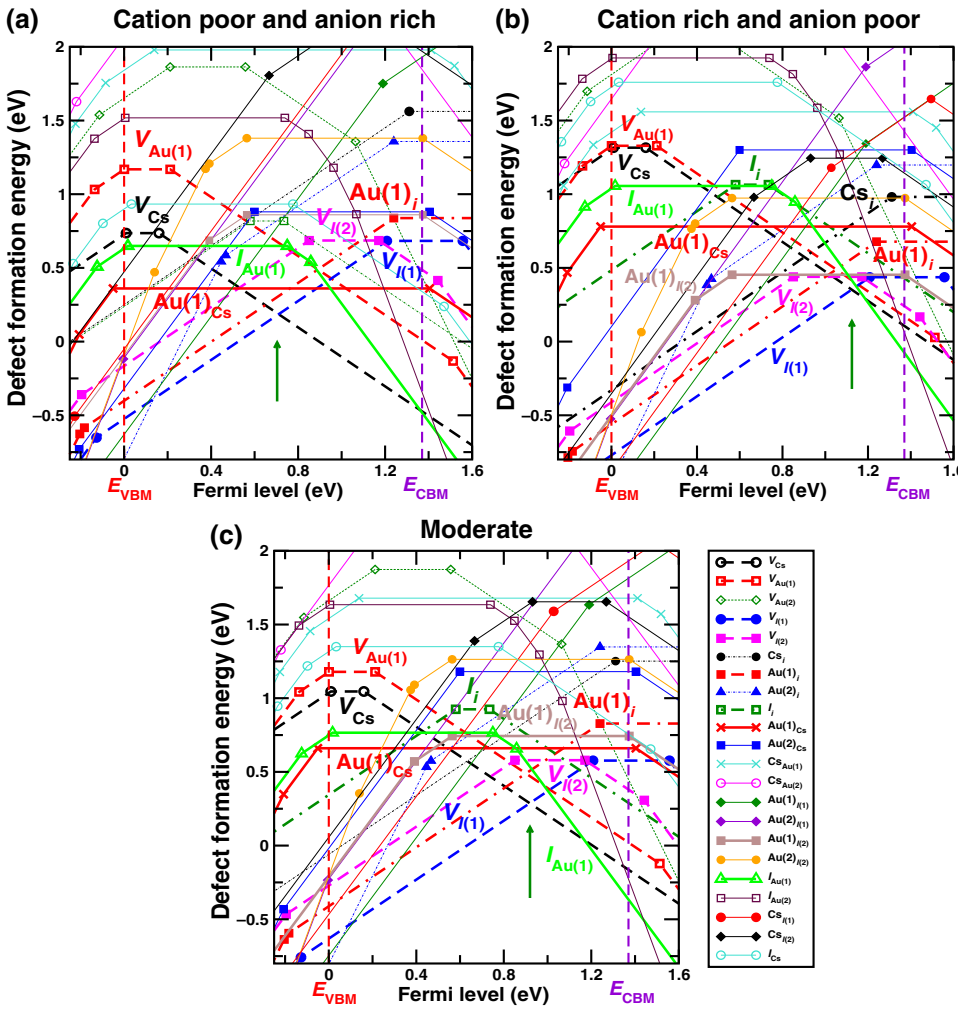


FIG. 3. Phase diagram (allowed chemical-potential regions for constituents) for (a) $\text{Cs}_2\text{Au}_2\text{I}_6$ and (b) $\text{Cs}_2\text{Au}_2\text{Br}_6$, with respect to competing elemental, binary, and ternary compounds. The brown-shaded regions show the stable region for these double perovskite halides (a zoomed view is shown in the inset). The stable regions for the competing phases are shown by the differently colored lines and the spaces on the side of those lines in the direction opposite to the shaded region.



and that $V_{I(1)}$ is more probable than $V_{I(2)}$. Apart from these, there are other possible defects which are likely to dominate depending on the chemical environment. These defects show deep transition levels well in the band gap, and may act as SRH recombination centers, hindering the photovoltaic efficiency. In the case of the bromide compound, vacancies at the two inequivalent halogen sites show different formation energies, with $V_{Br(2)}$ being the more probable one. In a cation-poor and anion-rich environment [Fig. 5(a)], the contribution from the acceptor V_{Cs} will be mainly compensated by donors $V_{Br(2)}$ and $Au(1)_i$, pinning the Fermi level on the *p*-type side of the band gap. At this Fermi-level pinning, a number of other deep-level donor defects [such as $Au(2)_{Cs}$, $Au(2)_{Br(2)}$, and $Au(2)_i$, $V_{Br(1)}$] and the acceptor $V_{Au(1)}$ are likely to form. A very low *n*-type concentration is expected under cation-rich and anion-poor growth conditions [see Fig. 5(b)]. Most of the defects will still be present when a moderate cation and anion environment is maintained [Fig. 5(c)], pinning the Fermi level in the middle of the band gap. In all these growth environments, the Fermi-level

FIG. 4. Defect formation energy as a function of Fermi level (E_F) for $Cs_2Au_2I_6$, for three different growth conditions: (a) cation poor and anion rich, (b) cation rich and anion poor, and (c) moderate cations and anions. In the phase diagram, these conditions are represented by points *A*, *E*, and *G*, respectively. According to Eq. (1), the charge state q of the defect is denoted by the slope of the function, and the Fermi level at the turning point gives the charge-transition energy level. Here each charge-transition point for a donor (acceptor) defect is indicated via filled (open) symbols. The regions to the left of E_{VBM} and to the right of E_{CBM} represent the valence band below the VBM and the conduction band above the CBM, respectively. The green arrows point toward the Fermi-level pinning.

pinning is mostly positioned near the midgap region, which explains the experimental observation of high resistivity in these compounds [24].

The overall analysis of these two halides from the perspective of stability (phase diagram) and defect tolerance indicates that the utmost care needs to be taken in synthesizing these compounds because the single-phase stability regions for both of them are rather small. In addition, both compounds show the possibility of numerous deep-level defects [even more so given the high-temperature (~ 900 K) synthesis procedure reported in [24]], which may act as carrier traps and thus substantially reduce V_{OC} in practice. As such, in spite of their excellent optoelectronic properties, $Cs_2Au_2X_6$ may have limited photovoltaic performance due to the possibility of deep-level defects. Nevertheless, there exist a few well-known compounds, such as CIGS and CZTS, where the formation of defect complexes has been reported to make deep-level defects electrically benign [32]. In the case of gold mixed halides, a number of defect complexes are possible, thus requiring further studies to get a deeper understanding.

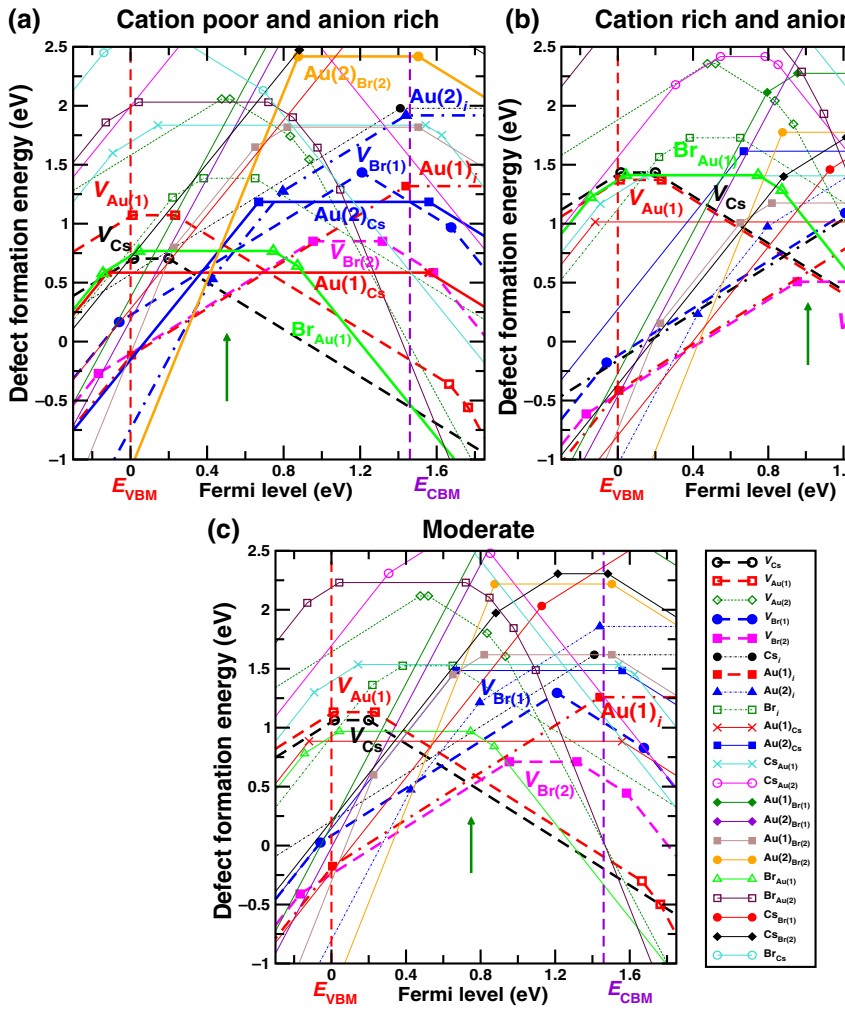


FIG. 5. Defect formation energy as a function of Fermi level (E_F) for $\text{Cs}_2\text{Au}_2\text{Br}_6$, for three different growth conditions: (a) cation poor and anion rich, (b) cation rich and anion poor, and (c) moderate cations and anions. In the phase diagram, these conditions are represented by points A, D, and G, respectively. According to Eq. (1), the charge state q of the defect is denoted by the slope of the function, and the Fermi level at the turning point gives the charge-transition energy level. Here each charge-transition point for a donor (acceptor) defect is indicated via filled (open) symbols. The regions to the left of E_{VBM} and to the right of E_{CBM} represent the valence band below the VBM and the conduction band above the CBM, respectively. The green arrows point toward the Fermi-level pinning.

VI. CONCLUSION

In summary, we carry out a detailed analysis of the optoelectronic properties and defect physics of $\text{Cs}_2\text{Au}_2X_6$ ($X = \text{I}, \text{Br}$), two compounds with several favorable properties such as nontoxicity, better stability, and high simulated efficiency. First-principles simulations predict these compounds to have a slightly indirect nature of the band gap, with the optically allowed direct band gap remaining very close (within 20 meV) to the indirect gap, allowing the optical absorption to be very high. The value of the band gap, falling in the visible region, and the sharp rise in the absorption coefficient near the band edge yield reasonably high simulated efficiency (even from a very small film thickness). Our study of defect physics, however, predicts the possibility of deep-level defects in both of these materials. Halide vacancies are observed to be the most dominant defects. Cation vacancies ($V_{\text{Cs}}, V_{\text{Au}(1)}$), interstitials, and a few antisite defects will also form, depending on the material and the growth environment. The existence of deep-level defects (which can act as trap states) will probably make the materials prone to carrier loss due to nonradiative recombination. Analysis of the defect physics (Fermi-level

pinning, dominant defects, etc.) explains some of the experimental observations reported earlier. Nevertheless, we believe that the present study will guide experimentalists in employing optimal chemical growth conditions to carry out future studies on these compounds and also help theoreticians to work on similar aspects of related materials [38–42].

ACKNOWLEDGMENTS

J.K. and S.G. have contributed equally to this work. They acknowledge financial support from IIT Bombay for a research fellowship. A.A. and M.A. acknowledge the National Center for Photovoltaic Research and Education (NCPRE), funded by the Ministry of New Renewable Energy (MNRE), the Government of India, and IIT Bombay to support this research.

APPENDIX A: COMPUTATIONAL DETAILS

All the calculations are done using DFT [20] as implemented in VASP [21,22] with the projector-augmented-wave basis set. Finding the equilibrium

structure, calculation of the decomposition enthalpy, and other primary electronic-structure calculations (band structure, density of states, etc.) were done using the PBE exchange-correlation functional [35]. Cs ($5s^25p^66s^1$), Au ($5d^{10}6s^1$), I ($5s^25p^5$), Br ($4s^24p^5$), Cl ($3s^23p^5$), C ($2s^22p^2$), N ($2s^22p^3$), and H ($1s^1$) are used as valence electrons. An energy cutoff of 500 eV with a $6 \times 6 \times 6$ Γ -centered k -mesh is considered for structural optimization, and unit cells are relaxed until the forces reach a value less than 0.001 eV/ \AA for $\text{Cs}_2\text{Au}_2X_6$, $X = \text{I}, \text{Br}, \text{Cl}$. For organic gold halides, we replace the Cs with MA (CH_3NH_3) and FA ($\text{CH}(\text{NH}_2)_2$) cations in the relaxed $\text{Cs}_2\text{Au}_2\text{I}_6$ structure and then relax the structure in three steps. First, we perform full geometrical relaxation, then again perform relaxation with parameters keeping the volume and shape fixed, and finally perform full geometrical relaxation with a cutoff of 500 eV with $6 \times 6 \times 6$ k -points until the forces converge to 0.01 eV/ \AA . Charge densities are calculated using an energy cutoff of 450 eV and an $8 \times 8 \times 8$ k -mesh using the relaxed structures until the energy converges to 10^{-6} eV. Next, we use the HSE06 [27] functional to get the band-edge information. To obtain a more accurate value of the band gap, we use the G_0W_0 method along with the HSE06 functional and the PBE exchange-correlation functional. Optical absorption coefficients are calculated within the independent-particle approximation with the PBE exchange-correlation functional and then scissor shifted to the experimental band gap while calculating the SLME. For simulation of various defects in different charge states, we use a 520 eV plane wave energy cutoff along with a gamma-centered k -mesh. For each defect in different charge states, we relax only the ionic positions, keeping the cell shape and volume fixed.

APPENDIX B: CORRECTIONS ASSOCIATED WITH CHARGED DEFECTS AND BAND-GAP UNDERESTIMATION

For charged defects, there are a few sources of error that come from the DFT approximation, which uses a background charge to neutralize the supercell. This requires two corrections: one is an electrostatic-interaction-term correction, and the other is a potential-alignment term. We use the well-documented Freysoldt, Neugebauer, and Van de Walle scheme to correct these errors [34]. Next we notice that for both of the halides, the PBE functional underestimates the band gap substantially. In practice, this can be seen as a shift of the VBM (CBM) up (down) by ΔE_{VBM} (ΔE_{CBM}) and a reduced band gap. This induces an underestimation of the defect formation energy by ΔE_{VBM} (ΔE_{CBM}) per hole (electron) occupying the acceptor (donor) level, in the case of acceptor- (donor-) type defects. Here, to correct these, we calculate the shift in the band edges from quasiparticle G_0W_0 calculations, which reproduce the experimental band gap very well in the case

of these two halides [36]. We calculate ΔE_{VBM} (ΔE_{CBM}) to be 0.39 eV (0.26 eV) in the case of $\text{Cs}_2\text{Au}_2\text{I}_6$ and 0.49 eV (0.30 eV) for $\text{Cs}_2\text{Au}_2\text{Br}_6$. All the defect-formation-energy calculations include the above-mentioned corrections.

Note: We use the same set of pseudopotentials for all the defect-related calculations, including phase diagrams and band-edge shifts.

APPENDIX C: CHOICE OF DEFECTS

Three types of defects are considered, vacancies ($V_{\text{Cs}}, V_{\text{Au}}, V_X$), interstitials ($\text{Cs}_i, \text{Au}_i, X_i$), and antisites ($\text{Cs}_{\text{Au}}, \text{Cs}_X, \text{Au}_{\text{Cs}}, \text{Au}_X, X_{\text{Cs}}, X_{\text{Au}}$) ($X = \text{I}, \text{Br}$). For these compounds, there are two inequivalent Wyckoff positions for both the halides X and Au, which we consider when considering the vacancy and antisite defects. For the interstitials, we consider all possible positions and choose the final position based on the total energy calculated for the neutral charge state. As discussed earlier, we denote Au^{+1} and Au^{+3} by $\text{Au}(1)$ and $\text{Au}(2)$, respectively. $X(1)$ and $X(2)$ ($X = \text{Br}, \text{I}$) represent halide anions at the 4e and 8h Wyckoff sites, respectively. Here, we use the PYCDT code [43] to generate the supercells with defects. To accurately calculate the various defect charge-state energies, a 160-atom supercell is used.

- [1] A. Kojima, K. Teshima, Y. Shirai, and T. Miyasaka, Organometal halide perovskites as visible-light sensitizers for photovoltaic cells, *J. Am. Chem. Soc.* **131**, 6050 (2009).
- [2] J. Qian, B. Xu, and W. Tian, A comprehensive theoretical study of halide perovskites ABX_3 , *Org. Electron.* **37**, 61 (2016).
- [3] W.-J. Yin, J.-H. Yang, J. Kang, Y. Yan, and S.-H. Wei, Halide perovskite materials for solar cells: A theoretical review, *J. Mater. Chem. A* **3**, 8926 (2015).
- [4] L. A. Frolova, D. V. Anokhin, K. L. Gerasimov, N. N. Dremova, and P. A. Troshin, Exploring the effects of the Pb^{2+} substitution in MAPbI_3 on the photovoltaic performance of the hybrid perovskite solar cells, *J. Phys. Chem. Lett.* **7**, 4353 (2016).
- [5] A. Kumar, K. Balasubramaniam, J. Kangsabanik, Vikram, and A. Alam, Crystal structure, stability, and optoelectronic properties of the organic-inorganic wide-band-gap perovskite $\text{CH}_3\text{NH}_3\text{BaI}_3$: Candidate for transparent conductor applications, *Phys. Rev. B* **94**, 180105 (2016).
- [6] N. K. Noel, S. D. Stranks, A. Abate, C. Wehrenfennig, S. Guarnera, A.-A. Haghimirad, A. Sadhanala, G. E. Eperon, S. K. Pathak, M. B. Johnston, A. Petrozza, L. M. Herz, and H. J. Snaith, Lead-free organic-inorganic tin halide perovskites for photovoltaic applications, *Energy Environ. Sci.* **7**, 3061 (2014).
- [7] T. Yokoyama, D. H. Cao, C. C. Stoumpos, T.-B. Song, Y. Sato, S. Aramaki, and M. G. Kanatzidis, Overcoming short-circuit in lead-free $\text{CH}_3\text{NH}_3\text{SnI}_3$ perovskite solar cells via kinetically controlled gas-solid reaction film fabrication process, *J. Phys. Chem. Lett.* **7**, 776 (2016).

- [8] G. Volonakis, M. R. Filip, A. A. Haghhighirad, N. Sakai, B. Wenger, H. J. Snaith, and F. Giustino, Lead-free halide double perovskites via heterovalent substitution of noble metals, *J. Phys. Chem. Lett.* **7**, 1254 (2016).
- [9] S. Chakraborty, W. Xie, N. Mathews, M. Sherburne, R. Ahuja, M. Asta, and S. G. Mhaisalkar, Rational design: A high-throughput computational screening and experimental validation methodology for lead-free and emergent hybrid perovskites, *ACS Energy Lett.* **2**, 837 (2017).
- [10] W. Meng, X. Wang, Z. Xiao, J. Wang, D. B. Mitzi, and Y. Yan, Parity-forbidden transitions and their impacts on the optical absorption properties of lead-free metal halide perovskites and double perovskites, *J. Phys. Chem. Lett.* **8**, 2999 (2017).
- [11] Z. Xiao, K.-Z. Du, W. Meng, J. Wang, D. B. Mitzi, and Y. Yan, Intrinsic instability of $\text{Cs}_2\text{In}(\text{I})\text{M(III)}\text{X}_6$ ($\text{M} = \text{Bi}, \text{Sb}$; $\text{X} = \text{Halogen}$) double perovskites: A combined density functional theory and experimental study, *J. Am. Chem. Soc.* **139**, 6054 (2017).
- [12] A. H. Slavney, L. Leppert, D. Bartesaghi, A. Gold-Parker, M. F. Toney, T. J. Savenije, J. B. Neaton, and H. I. Karunadasa, Defect-induced band-edge reconstruction of a bismuth-halide double perovskite for visible-light absorption, *J. Am. Chem. Soc.* **139**, 5015 (2017).
- [13] T. T. Tran, J. R. Panella, J. R. Chamorro, J. R. Morey, and T. M. McQueen, Designing indirect-direct bandgap transitions in double perovskites, *Mater. Horiz.* **4**, 688 (2017).
- [14] J. Kangsabanik, V. Sugathan, A. Yadav, A. Yella, and A. Alam, Double perovskites overtaking the single perovskites: A set of new solar harvesting materials with much higher stability and efficiency, *Phys. Rev. Mater.* **2**, 055401 (2018).
- [15] X. Liu, K. Matsuda, Y. Moritomo, A. Nakamura, and N. Kojima, Electronic structure of the gold complexes $\text{Cs}_2\text{Au}_2\text{X}_6$ ($\text{X} = \text{I}, \text{Br}$, and Cl), *Phys. Rev. B* **59**, 7925 (1999).
- [16] N. Kojima and N. Matsushita, P-T phase diagram and Au valence state of the perovskite-type Au mixed-valence complexes $\text{M}_2[\text{Au}^{\text{I}}\text{X}_2][\text{Au}^{\text{III}}\text{X}_4]$ ($\text{M} = \text{K}, \text{Rb}, \text{Cs}$; $\text{X} = \text{Cl}, \text{Br}, \text{I}$), *Coord. Chem. Rev.* **198**, 251 (2000).
- [17] L. Debbichi, S. Lee, H. Cho, A. M. Rappe, K.-H. Hong, M. S. Jang, and H. Kim, Mixed valence perovskite $\text{Cs}_2\text{Au}_2\text{I}_6$: A potential material for thin-film Pb-free photovoltaic cells with ultrahigh efficiency, *Adv. Mater.* **30**, 1707001 (2018).
- [18] G. Giorgi, K. Yamashita, and M. Palummo, Two-dimensional optical excitations in the mixed-valence $\text{Cs}_2\text{Au}_2\text{I}_6$ fully inorganic double perovskite, *J. Mater. Chem. C* **6**, 10197 (2018).
- [19] A. Walsh and A. Zunger, Instilling defect tolerance in new compounds, *Nat. Mater.* **16**, 964 (2017).
- [20] W. Kohn and L. J. Sham, Self-consistent equations including exchange and correlation effects, *Phys. Rev. A* **140**, 1133 (1965).
- [21] G. Kresse and J. Furthmüller, Efficiency of Ab-initio total energy calculations for metals and semiconductors using a plane-wave basis set, *Comput. Mater. Sci.* **6**, 15 (1996).
- [22] G. Kresse and D. Joubert, From ultrasoft pseudopotentials to the projector augmented-wave method, *Phys. Rev. B* **59**, 1758 (1999).
- [23] See the Supplemental Material, <http://link.aps.org/supplemental/10.1103/PhysRevApplied.13.014005> in which a brief formalism for calculating the dielectric constants is given in Sec. III.A, which includes Ref. [38]. It also contains details of the stability of different materials, further electronic-structure data, transition probabilities, further optical data, and defect properties under different growth conditions. In Sec. III.B, a brief discussion of the SLME can be found, which includes Ref. [39–42].
- [24] S. C. Riggs, M. Shapiro, F. Corredor, T. Geballe, I. Fisher, G. T. McCandless, and J. Y. Chan, Single crystal growth by self-flux method of the mixed valence gold halides $\text{Cs}_2[\text{Au}^{\text{I}}\text{X}_2][\text{Au}^{\text{III}}\text{X}_4]$ ($\text{X} = \text{Br}, \text{I}$), *J. Cryst. Growth* **355**, 13 (2012).
- [25] M. R. Filip and F. Giustino, G W quasiparticle band gap of the hybrid organic-inorganic perovskite $\text{CH}_3\text{NH}_3\text{PbI}_3$: Effect of spin-orbit interaction, semicore electrons, and self-consistency, *Phys. Rev. B* **90**, 245145 (2014).
- [26] M. Born and K. Huang, *Dynamical Theory of Crystal Lattices* (Oxford University Press, London, 1954).
- [27] A. V. Kruckau, O. A. Vydrov, A. F. Izmaylov, and G. E. Scuseria, Influence of the exchange screening parameter on the performance of screened hybrid functionals, *J. Chem. Phys.* **125**, 224106 (2006).
- [28] N. Kojima and H. Kitagawa, Optical investigation of the intervalence charge-transfer interactions in the three-dimensional gold mixed-valence compounds $\text{Cs}_2\text{Au}_2\text{X}_6$ ($\text{X} = \text{Cl}, \text{Br}$ or I), *J. Chem. Soc. Dalton Trans.* **3**, 327 (1994).
- [29] J. Heo, L. Yu, E. Altschul, B. E. Waters, J. F. Wager, A. Zunger, and D. A. Kesler, CuTaS₃: Intermetal d-d transitions enable high solar absorption, *Chem. Mater.* **29**, 2594 (2017).
- [30] H. A. Evans, E. C. Schueller, S. R. Smock, G. Wu, R. Seshadri, and F. Wudl, Perovskite-related hybrid noble metal iodides: Formamidinium platinum iodide $[(\text{FA})_2\text{Pt}^{\text{IV}}\text{I}_6]$ and mixed-valence methylammonium gold iodide $[(\text{MA})_2\text{Au}^{\text{I}}\text{Au}^{\text{III}}\text{I}_6]$, *Inorganica Chim. Acta* **468**, 280 (2017).
- [31] S. K. Wallace, D. B. Mitzi, and A. Walsh, The steady rise of kesterite solar cells, *ACS Energy Lett.* **2**, 776 (2017).
- [32] J. S. Park, S. Kim, Z. Xie, and A. Walsh, Point defect engineering in thin-film solar cells, *Nat. Rev. Mater.* **3**, 194 (2018).
- [33] W.-J. Yin, T. Shi, and Y. Yan, Unusual defect physics in $\text{CH}_3\text{NH}_3\text{PbI}_3$ perovskite solar cell absorber, *Appl. Phys. Lett.* **104**, 063903 (2014).
- [34] C. Freysoldt, J. Neugebauer, and C. G. Van de Walle, Fully Ab Initio Finite-size Corrections for Charged-Defect Super-cell Calculations, *Phys. Rev. Lett.* **102**, 016402 (2009).
- [35] J. P. Perdew, K. Burke, and M. Ernzerhof, Generalized Gradient Approximation Made Simple, *Phys. Rev. Lett.* **77**, 3865 (1996).
- [36] S. Lany and A. Zunger, Assessment of correction methods for the band-gap problem and for finite-size effects in supercell defect calculations: Case studies for ZnO and GaAs, *Phys. Rev. B* **78**, 235104 (2008).
- [37] A. Jain, S. P. Ong, G. Hautier, W. Chen, W. D. Richards, S. Dacek, S. Cholia, D. Gunter, D. Skinner, and G. Ceder, Commentary: The materials project: A materials genome approach to accelerating materials innovation, *APL Mater.* **1**, 011002 (2013).

- [38] M. Gajdoš, K. Hummer, G. Kresse, J. Furthmüller, and F. Bechstedt, Linear optical properties in the projector-augmented wave methodology, *Phys. Rev. B* **73**, 045112 (2006).
- [39] L. Yu and A. Zunger, Identification of Potential Photovoltaic Absorbers based on First-principles Spectroscopic Screening of Material, *Phys. Rev. Lett.* **108**, 068701 (2012).
- [40] W. Shockley and H. J. Queisser, Detailed balance limit of efficiency of p-n junction solar cells, *J. Appl. Phys.* **32**, 510 (1961).
- [41] M. A. Green, Third generation photovoltaics: Advanced solar energy conversion, *Phys. Today* **57**, 71 (2004).
- [42] T. Tiedje, E. Yablonovitch, G. D. Cody, and B. G. Brooks, Limiting efficiency of silicon solar cells, *IEEE Trans. Electron Devices* **31**, 711 (1984).
- [43] D. Broberg, B. Medasani, N. E. Zimmermann, G. Yu, A. Canning, M. Haranczyk, M. Asta, and G. Hautier, PyCDT: A Python toolkit for modeling point defects in semiconductors and insulators, *Comput. Phys. Commun.* **226**, 165 (2018).